Heliyon 10 (2024) e37513

Contents lists available at ScienceDirect

Heliyon

journal homepage: www.cell.com/heliyon

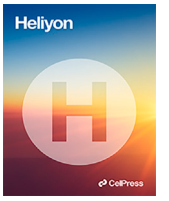

Research article

Subnanosecond visible two-stage optical parametric generator and amplifier based on MgO:PPLN and LBO crystals at strong pump depletion

V. Tamulienė *, G. Stanionytė, T. Latvys, J. Vengelis

Laser Research Center, Vilnius University, Vilnius, LT-10223, Lithuania

ARTICLE INFO

Keywords:
Optical parametric generation
Optical parametric amplification
Subnanosecond pulses
Numerical simulation

ABSTRACT

Theoretical and experimental investigation of two-stage optical parametric generator based on magnesium oxide doped periodically poled lithium niobate (MgO:PPLN) crystal and optical parametric amplifier based on lithium triborate (LBO) crystal is presented. The first stage crystal was pumped by the subnanosecond fundamental harmonic at 1064 nm wavelength. In the theoretical description, the input signal and idler photons are described by the quantum model and their further amplification is tracked by simulating the nonlinear coupling equations. Such description allows the analysis of pulsed beam evolution during the propagation in the nonlinear crystal under strong pump depletion regime. The second stage crystal was seeded by the output signal wave of the first stage and pumped by the third harmonic of the laser radiation. Experimentally, tuning in the visible wavelength ranges and high pulse power (up to 20 mW at 475 nm wavelength) were achieved.

1. Introduction

Subnanosecond pulses (duration 300 ps – 1 ns) delivered by compact and cost-efficient Q-switched microlasers (or microchip lasers) [1,2] can be used in different research and application areas [3] such as laser induced breakdown spectroscopy [4], supercontinuum generation [5] and nonlinear optics [6]. Optical parametric generation (OPG), optical parametric amplification (OPA) and optical parametric oscillation (OPO) of subnanosecond pulses may provide a tunable wavelength radiation which is a cheaper and more robust alternative to the ultrashort femtosecond parametric systems in the case when the femtosecond resolution is not required. Compared to nanosecond parametric systems which are of higher spectral resolution, subnanosecond OPGs and OPAs deliver much higher output peak powers.

Numerous recent studies of the subnanosecond OPGs and OPAs [7–10] as well as OPOs [11] demonstrated the generation and amplification of subnanosecond pulses in the infrared wavelength ranges. Pumped by the fundamental harmonic of the laser at 1064 nm wavelength, the signal output is typically tuned in the range of about 1.5 μm – 2 μm wavelengths. In the visible wavelength range, the first OPG at 220 ps pulse duration was demonstrated in [12] where the periodically poled lithium niobate crystal was pumped by the second harmonic of the laser at 532 nm wavelength. The pulse energies of about one microjoule were achieved.

In this work, we investigate a two-stage parametric system based on magnesium oxide doped periodically poled lithium niobate (MgO:PPLN) OPG crystal and lithium triborate (LBO) OPA crystal for the generation of the visible subnanosecond radiation at high

* Corresponding author.
E-mail address: viktorija.tamuliene@ff.vu.lt (V. Tamulienė).

https://doi.org/10.1016/j.heliyon.2024.e37513
Received 25 June 2024; Received in revised form 16 August 2024; Accepted 4 September 2024

Available online 6 September 2024

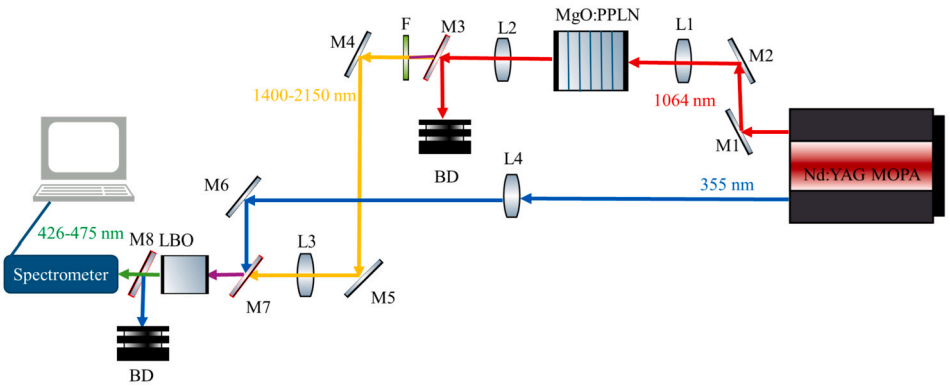

Fig. 1. Experimental setup. M1, M2 – 1064 nm mirrors (AOI = 45°), L1, L2, L3, L4 – lenses, MgO:PPLN – magnesium oxide doped periodically poled lithium niobate ($LiNbO_3$) crystal, BD – beam damper, M3 – mirror, HR@532 nm + 1064 nm, HT@1410-2128 nm, F – filters, IKS7 and FB1750–500 (ThorLabs), M4, M5 – gold mirrors, M6, M8 – mirrors, λ = 351 – 361 nm (AOI = 45°), M7 – mirror, HR@355 nm, HT@700 – 2200 nm (AOI = 45°), LBO – lithium triborate crystal.

conversion efficiency regime. The study is both theoretical and experimental. The particular theoretical description is required due to the high conversion efficiency and pump depletion during the first-stage OPG process. We note, that OPG is seeded by the quantum-noise signal and idler waves and the quantum model [13,14] is suitable for the not depleted monochromatic pump wave. The assumption of constant pump field fails at the high-conversion efficiency and subsequent strong pump depletion. In this work, at initial propagation length, the quantum-noise seed is described from the quantum model [14] and the further propagation is simulated by the use of three-wave nonlinear coupling equations. The choice of the initial length is demonstrated to be not crucial as far as the pump depletion does not take place at this length. Note that in [15], the 'critical length' as the length where the first signal and idler photons are generated was involved into theoretical model of picosecond OPG pumped by 532 nm wavelength radiation. In the present work, the simulation of the nonlinear coupling equations allowed the tracking of the pulsed beams evolution for three interacting waves. Then, the second stage OPA crystal is seeded by the output OPG infrared signal wave and it is pumped by the third harmonic of microchip laser (wavelength 355 nm). Such configuration yields a tunable visible subnanosecond OPA signal radiation of energy up to 20 microjoules. The main focus of this paper is to simulate the OPG process with inclusion of the pump depletion and to track the signal wave evolution during propagation in both first and second stage crystals. Some important aspects like conical beam formation in the MgO:PPLN OPG crystal and their possible influence to the laser-induced damage threshold (LIDT) are revealed.

2. Experimental setup

Experimental setup is presented in Fig. 1. The pump source is a passively Q-switched Nd:YAG MOPA microlaser (manufactured by *Standa Ltd*) with first/fundamental (λ = 1064 nm), second (λ = 532 nm) and third (λ = 355 nm) harmonic outputs delivering subnanosecond (around 500 ps) duration pulses with 1 kHz repetition rate. Maximum pulse energy of the harmonic outputs was 75 μJ, 75 μJ and 100 μJ for the first, second and third harmonics respectively. One should distinguish two stages in the setup: the first stage of optical parametric generator (OPG) based on MgO:PPLN crystal and the second stage of optical parametric amplifier (OPA) based on LBO crystal.

In the first stage the fundamental harmonic beam was focused with a f = 75 mm focal length lens L1 into a 5% MgO:PPLN crystal (1 cm width, 0.5 cm height and 5 cm thickness) where signal and idler waves were generated (an OPG setup). The MgO:PPLN crystal was uncoated and produced by *HC Photonics*. It had grating periods of Λ = 27.58; 27.91; 28.28; 28.67; 29.08; 29.52; 29.98; 30.49; 31.02 and 31.59 μm and was mounted in an oven which could heat up to 200 °C with 0.1 °C precision. The oven was controlled with a temperature controller ("HC Photonics", TC038–PC) and mounted on a translation stage which enabled easy and precise changing of crystal gratings by moving the crystal in direction perpendicular to pump beam propagation direction. The generated waves were collimated using another f = 75 mm focal length lens L2. The generated signal wave was used as seed source for the LBO OPA thus spectral separator mirror M3 and filters IKS7 and FB1750–500 (*ThorLabs*) F were used to filter out the idler and remaining pump radiation.

In the second stage a LBO crystal (9 mm width, 6 mm height and 15 mm thickness) cut at θ = 90° and ϕ = 30.3° for type I phase matching and covered with antireflection coatings at 355 nm and 400-760 nm wavelengths was pumped by the third harmonic of the Nd:YAG MOPA microlaser (λ = 355 nm) and seeded by the signal wave from the MgO:PPLN OPG (wavelengths from 1400 nm to 2150 nm). Pump and seed radiation were focused separately (see Fig. 1): a f = 250 mm focal length lens L4 was used to focus the pump beam while a f = 125 mm focal length lens L3 was used to focus the seed beam. Moreover, pump and seed pulses were matched in time (by placing mirror M6 at a certain distance) for maximum conversion efficiency. Angular phase matching was used to tune the wavelength of the generated wave (which we will refer to as the signal wave as it has shorter wavelength (greater frequency) than the seed radiation of the OPA). We managed to achieve signal wavelength tuning from 426 nm to 475 nm (corresponds to LBO crystal phase matching angles θ_{ph} = 22.5°–31.5°) when using the aforementioned seed radiation, but we also realized wavelength tuning in the 532-710 nm spectral range (corresponds to LBO crystal phase matching angles θ_{ph} = 37.1°–42°) by employing second harmonic

Table 1
Parameters of pump radiation and nonlinear medium at the first (OPG) stage.

Parameter	Value	Description
T	$180\,^{\circ}C$	Crystal temperature
d_{eff}	17 pm/V	Effective nonlinear susceptibility
d_3	50 μm	Pump beam radius
τ_3	400 ps	Pump pulse duration
λ_{30}	1064 nm	Pump wavelength
P_3	70 mW	Pump power
f_{rep}	1 kHz	Repetition frequency

of the MgO:PPLN signal wave as seed radiation. However, we focused numerical simulations on the 426-475 nm wavelength range, so that additional second harmonic stage is not depicted in Fig. 1.

In the following Sections, we describe both the theoretical and experimental results delivered from these two stages.

3. First stage: OPG based on MgO:PPLN crystal

To analyze the three-wave propagation in nonlinear crystal under strong pump depletion, we simulated the three-wave coupling equations for the Fourier transforms $S_j(k_x, k_y, \Omega)$ of the complex amplitudes $A_j(x, y, t)$, where $j = 1$, 2 and 3 denote signal, idler and pump waves, respectively. x, y, z are the Cartesian coordinates with z being the longitudinal propagation coordinate and t is time. The equations read:

$$\frac{\partial S_1}{\partial z} = i\left(k_1' - k_{10} - \frac{k_x^2 + k_y^2}{2k_{10}}\right) S_1 + \sigma_1 \mathrm{FT}(A_2^* A_3), \tag{1}$$

$$\frac{\partial S_2}{\partial z} = i\left(k_2' - k_{20} - \frac{k_x^2 + k_y^2}{2k_{20}}\right) S_2 + \sigma_2 \mathrm{FT}(A_1^* A_3), \tag{2}$$

$$\frac{\partial S_3}{\partial z} = i\left(k_3' - k_{30} - \frac{k_x^2 + k_y^2}{2k_{30}}\right) S_3 - \sigma_3 \mathrm{FT}(A_1 A_2), \tag{3}$$

where $i = \sqrt{-1}$, $k_j' = k_j - \Omega/u_{30}$, $k_j = \frac{2\pi n_j(\lambda_j, T)}{\lambda_j}$ is the wavelength-dependent wavenumber, $\lambda_j = \frac{2\pi c}{\omega_j}$ is the wavelength of jth wave, ω_j is its angular frequency, T is the temperature and c is speed of light. u_{30} is the group velocity of the pump wave and the shift Ω/u_{30} represents the reference frame of the pump wave. In the case of noncritical ee-e interaction, n_j is the refractive index of the extraordinary wave, found by the use of the temperature-dependent Sellmeier equation for MgO:PPLN crystal [16]. Temperature value is given in Table 1. k_{j0} are calculated at the central wavelengths λ_{j0}. Term $k_j' - k_{j0}$ describes the linear pulse propagation in the dispersive medium, and $\frac{k_x^2 + k_y^2}{2k_{j0}}$ describes the beam diffraction. FT(∘) is the Fourier transform operation and $\sigma_j = \frac{d_{\mathrm{eff}}\omega_{j0}}{cn_{j0}}$ is the nonlinear coupling coefficient, indexes 0 represent the central wavelength, d_{eff} is the effective nonlinear susceptibility and its value is given in Table 1. The last rhs terms describe the nonlinear coupling.

The central wavelengths of the signal and idler waves are estimated by the use of the quasi-phase matching conditions:

$$\frac{1}{\lambda_{10}} + \frac{1}{\lambda_{20}} = \frac{1}{\lambda_{30}} \tag{4}$$

$$k_{30} - k_{10} - k_{20} = \frac{2\pi}{\Lambda}, \tag{5}$$

where Λ is the grating period of the MgO:PPLN crystal. Its value at temperature T was calculated by the use of the formula given in [16]. By the use of Eqs. (4) and (5) we calculated the phase-matching curve that is presented in Fig. 2. The first five available grating periods are marked by the black circles. Further, we will present the analysis of the numerical simulations performed for the first grating.

At initial longitudinal coordinate $z = 0$, the input pump wave is described by

$$A_{30}(x, y, t) = a_{30} \exp\left(-\frac{x^2 + y^2}{d_3^2}\right) \exp\left(-2\ln(2)\frac{t^2}{\tau_3^2}\right). \tag{6}$$

This is a subnanosecond Gaussian pulsed beam, see Table 1 for the values of the pulse duration τ_3 (at full width half maximum (FWHM)) and beam radius d_3 (at $1/e^2$ level). The central wavelength λ_{30} corresponds to the fundamental harmonic, Table 1. a_{30} is the peak amplitude and it was found when knowing the average power P_3 and repetition frequency f_{rep}, Table 1.

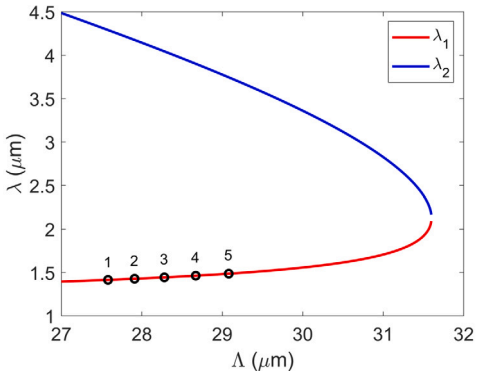

Fig. 2. Phase-matching curve for MgO:PPLN crystal. Black circles denote the first five gratings. Numerical simulation, first stage.

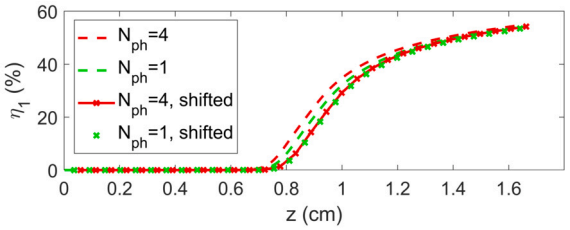

Fig. 3. Dependence of the conversion efficiency to the signal wave on the propagation distance. Dashed lines: the z axis without shift. Crosses: z axis shifted by L_i, Eq. (11). Two values of N_{ph} are compared. Numerical simulation, first stage.

The input signal and idler waves should mimic the quantum noise and we simulate them as independent random noise:

$$A_{10}(x,y,t) = a_{10}\xi_1(x,y,t), \tag{7}$$

$$A_{20}(x,y,t) = a_{20}\xi_2(x,y,t), \tag{8}$$

where $\xi_{1,2}$ are the random numbers at each space and time pixel of normal distribution with zero mean and unity standard deviation. The initial noise levels $a_{1,20}$ were estimated by the use of the quantum theory [14]. At small propagation distance $z = L_i$, we set the intensities of the signal and idler waves equal to:

$$I_{10} = \frac{c\hbar\omega_{20}}{2n_3 V}\left(\frac{\kappa_1}{g}\right)^2 \sinh^2(gL_i), \tag{9}$$

$$I_{20} = \frac{c\hbar\omega_{10}}{2n_3 V}\left(\frac{\kappa_2}{g}\right)^2 \sinh^2(gL_i), \tag{10}$$

where $\hbar$ is the reduced Planck constant, $g = \sqrt{\kappa_1\kappa_2^*}$, $\kappa_{1,2} = a_{30}\sigma_{1,2}$ (note, that in [14], Eqs. (11.98), (11.99), κ_2 should be replaced by κ_1 and vice versa). $V = L_i\pi d_3^2/2$ is the beam volume in the crystal. We estimate the initial propagation length L_i from the equation

$$N_{\text{ph}} = \sinh^2(gL_i), \tag{11}$$

where N_{ph} is the initial photon number and it should be not too large so that the depletion does not take place. We note, that the presented formulas are valid for the classical monochromatic undepleted pump wave. We will show, that at different photon numbers N_{ph} we achieve the same result.

The governing equations (1)–(3) with boundary conditions (6)–(8) were simulated by the use of the symmetrized Fourier split-step method [17]. The longitudinal step was equal to $h_z = \Lambda(T)/2$. The time domain $t \in [-2\tau,\ 2\tau)$ was divided to $n_t = 2^{13}$ equal steps, and the space domains $x, y \in [-8d_3,\ 8d_3)$ were divided to 64 equal steps.

In Fig. 3, we compare the effect of different values of initial photon number N_{ph}. Here, the simulated dependence of the conversion efficiency on the longitudinal propagation distance is presented. At larger value of N_{ph}, the amplification starts at smaller propagation distance, however, at the same time the shift L_i (see Eq. (11)) becomes larger. Therefore, when applying the appropriate shift, the curves at different N_{ph} numbers coincide. Further simulations were performed at $N_{\text{ph}} = 4$.

The simulated final propagation distance $z = 1.7$ cm was smaller than the experimental crystal length $L = 5$ cm. In Fig. 4, we intend to show that due to the saturation the smaller distance value was enough. In this Figure, the dependencies of the conversion efficiency and bandwidth on the propagation distance for both signal and idler waves are presented. As we can see, all the curves

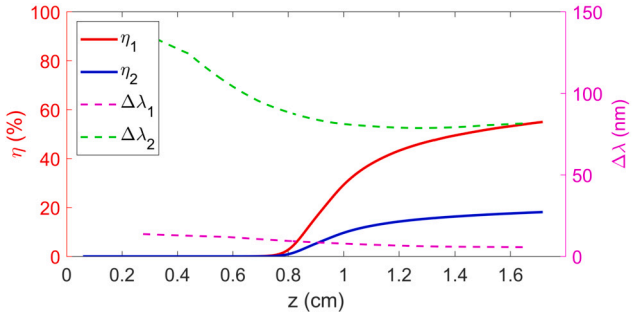

Fig. 4. Solid lines: dependence of the conversion efficiency to the signal (red line) and idler (blue line) waves on the propagation distance. Dashed lines: dependence of the signal (magenta line) and idler (green line) bandwidths (at FWHM) on the propagation distance. Numerical simulation, first stage.

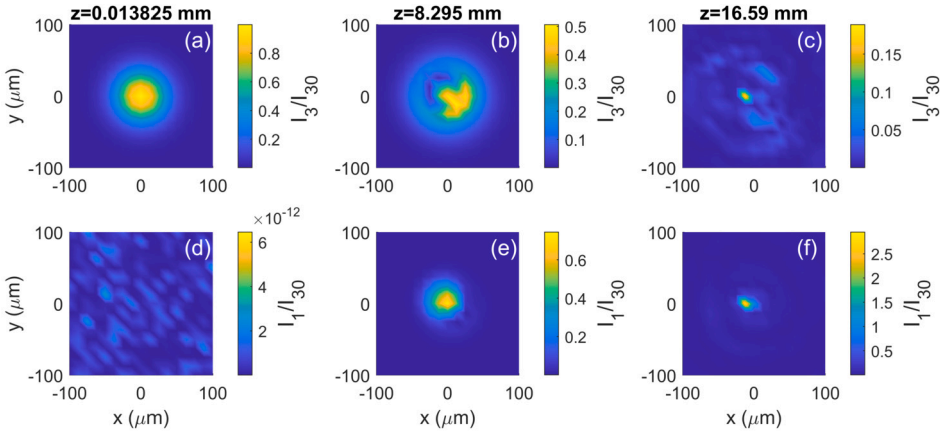

Fig. 5. Intensity profiles at $t = 0$ of pump (a,b,c) and signal (d,e,f) beams at three different propagation distance z values. z [mm]: 0.013825 (a,d); 8.295 (b,e); 16.59 (c,f). Numerical simulation, first stage.

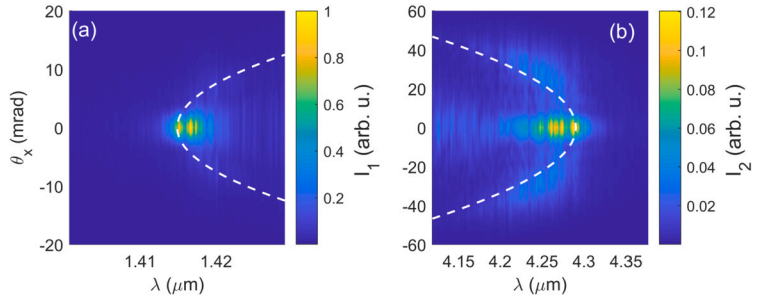

Fig. 6. Angular-frequency spectra at $\theta_y = 0$ of signal (a) and idler (b) waves at $z = 1.7$ cm. Dashed white lines correspond to the longitudinal phase-matching condition, see Eq. (12). Numerical simulation, first stage.

tend to saturate at $z = 1.7$ cm. Involving the experimental value of the propagation distance would be very time-consuming and the obtained numerical results would not differ significantly.

In Fig. 5, the beam profiles of pump (a–c) and signal (d–f) waves at different propagation length values are presented. As we can see, the pump starts from the Gaussian profile (a), then it gets strongly depleted (b) and finally, the profile obeys a sharp narrow maximum (c). This maximum is caused by the sharp maximum in the signal beam (f). The signal beam evolves from noisy distribution (d), then the smooth profile is generated (e) which becomes a sharp narrow maximum (f) with peak intensity higher than the initial pump peak intensity. This feature should be noted since it may influence the LIDT. The sharp maximum in the signal beam is caused by the conical structures in the angular spectrum. The profiles of the angular-frequency spectra of signal and idler waves are presented in Fig. 6. Here, the dashed white lines were calculated by the use of the longitudinal phase-matching condition that yields the parabola equation:

$$\Omega_{1,2} = \pm\frac{1}{2}(k_x^2 + k_y^2)\frac{1/k_{10} + 1/k_{20}}{1/u_{10} - 1/u_{20}}, \tag{12}$$

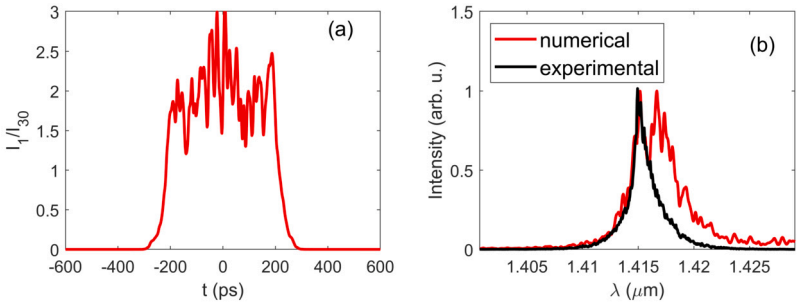

Fig. 7. Output signal pulse profile at $x = y = 0$ (a) and frequency spectrum at $\theta_x = \theta_y = 0$ (b). Red lines: numerical simulation. Black curve in (b): experimentally measured signal spectrum. First stage.

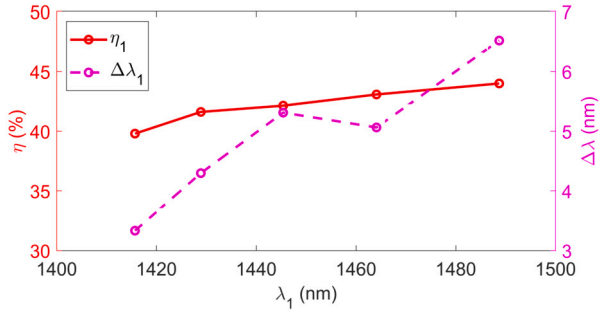

Fig. 8. Solid line: dependence of the conversion efficiency to the signal wave on the central wavelength. Dashed line: dependence of the signal bandwidth (RMS) on the central wavelength. Input pump power 68 mW. Experimental, first stage.

where '+' sign corresponds to the signal wave and '−' sign stands for the idler wave. Angle $\theta_x = k_x/k_{1,20}$. As we can see, at different wavelengths the signal and idler beams are conical with different cone angles. We note that the spontaneous generation of the Bessel (conical) beams during the traveling-wave optical parametric generation process was observed already in [18]. There, the pump pulse duration was 1 ps and the noncritical phase-matching was utilized.

The signal pulse profile and spectrum are presented in Fig. 7. The pulse duration is around 400 ps and calculated spectrum bandwidth is 5.4 nm (FWHM). The measured spectrum bandwidth was 3.3 nm (root mean square (RMS)). As we can see, the simulated spectrum has an additional peak which is due to the random noise in the boundary conditions (7) and (8). The experimental signal spectrum was measured with an optical spectrum analyzer "ANDO AQ6317C", while the output power was measured with "Ophir PD300-IRG-V1" power sensor. The crystal was heated in the oven (HC Photonics). In the experiment, the crystal length was $L = 5$ cm and other parameters were the same as in numerical simulation, Table 1. The measured conversion efficiency to signal wave and signal bandwidth (RMS) are presented in Fig. 8. Here, first five gratings are considered. At $\lambda = 462$ nm we can notice a small drop in generated pulse bandwidth which can be due to several reasons related to fluctuations of experimental conditions: MgO:PPLN crystal periodic quality reduction, wavelength dependent losses, etc. In the case of the first grating, the experimental conversion efficiency (about 40%) was smaller than the numerical one (about 54%, Fig. 4). This difference can be attributed to the simplification of the experimental conditions in the theoretical simulations. The experimental conversion efficiency is reduced by the idler wave losses at > 4 μm wavelength [19]. It would be a complicated task to take into account the wavelength-dependent losses into our model and therefore the simplified model without losses is presented.

4. Second stage: OPA based on LBO crystal

Next, we simulated the three-wave interaction equations accounting linear and nonlinear propagation in LBO crystal:

$$\frac{\partial S_1}{\partial z} = i\left(K_1' - K_{10} - \frac{k_x^2 + k_y^2}{2K_{10}} - \beta_3 k_x\right) S_1 + \widehat{N}_1, \tag{13}$$

$$\frac{\partial S_2}{\partial z} = i\left(K_2' - K_{20} - \frac{k_x^2 + k_y^2}{2K_{20}} - \beta_3 k_x\right) S_2 + \widehat{N}_2, \tag{14}$$

$$\frac{\partial S_3}{\partial z} = i\left(K_3' - K_{30} - \frac{k_x^2 + k_y^2}{2K_{30}}\right) S_3 - \widehat{N}_3, \tag{15}$$

Table 2
Parameters of pump radiation and nonlinear medium at the second (OPA) stage.

Parameter	Value	Description
d_{eff}	0.73 pm/V	Effective nonlinear susceptibility
θ_{ph}	31.07°	Phase matching angle
β_3	16.81 mrad	Walk-off angle
d_3	90 μm	Pump beam radius
τ_3	500 ps	Pump pulse duration
λ_{30}	355 nm	Pump wavelength
P_3	100 mW	Pump power
f_{rep}	1 kHz	Repetition frequency

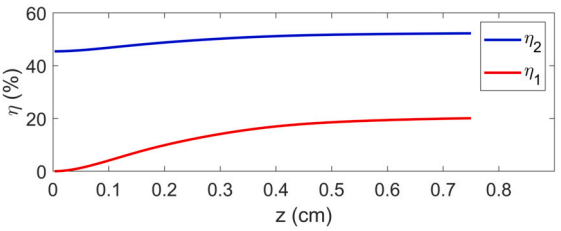

Fig. 9. Dependence of the conversion efficiency of the signal (red line) and idler (blue line) waves on the propagation distance. Numerical simulation, second stage.

where the Type-I (oo-e) phase matching in XY plane was assumed. The notations are analogous to the first stage ones. Here, $K_j' = K_j - \Omega/U_{30}$, $K_j = \frac{2\pi N_j(\lambda_j)}{\lambda_j}$, refractive indexes N_j were calculated by the use of the Sellmeier equations [20]. β_3 is the walk-off angle of the extraordinary pump wave; signal and idler waves are ordinary ones. The nonlinear coupling terms read: $\widehat{N}_1 = \sigma_1 \text{FT}(A_2^* A_3)$, $\widehat{N}_2 = \sigma_2 \text{FT}(A_1^* A_3)$ and $\widehat{N}_3 = \sigma_3 \text{FT}(A_1 A_2)$, where σ_j corresponds to the second stage wavelengths and effective nonlinear susceptibility d_{eff}. The parameters are given in Table 2. We note that although d_{eff} of LBO crystal is not very large, the walk-off parameter β_3 is also small when compared to other nonlinear crystals such as beta-barium borate (BBO) crystal. Now, the phase-matching conditions read

$$\frac{1}{\lambda_{10}} + \frac{1}{\lambda_{20}} = \frac{1}{\lambda_{30}} \tag{16}$$

$$K_{10} + K_{20} = K_{30}. \tag{17}$$

We note that in the second stage, the idler wavelength λ_{20} corresponds to the signal wavelength of the first stage λ_{10}, while the OPA pump wavelength λ_{30} is given in Table 2. As a result, the OPA signal wave at the new wavelength λ_{10} is generated (see Eq. (16)). In the case of the first grating, the calculated phase matching angle θ_{ph} value is given in Table 2.

At the second stage, the input pump wave is the Gaussian pulsed beam, given by Eq. (6) with new parameters inserted, Table 2. We set pump power to 100 mW which was the maximum available power of the MOPA laser. The second-stage seed $A_{20}(x, y, t)$ was given by the output field of the first stage $A_1(x, y, t)$ multiplied by the factor $\sqrt{n_1/N_2}$. The input second-stage signal wave $A_{10}(x, y, t)$ was set to zero.

Governing equations (13)–(15) with the described boundary conditions were simulated by the use of the symmetrized Fourier split-step method [17]. The longitudinal step was set to 1.5/500 cm and the space x, y domains as well as time t domain were the same as in the first stage.

In Fig. 9, the dependence of the conversion efficiency of signal and idler waves on the propagation length is presented. First first-stage OPG grating is considered. The corresponding OPA output signal beam profile and angular-frequency spectrum are depicted in Fig. 10. Due to the pump beam (extraordinary wave) space walk-off with respect to the signal and idler beams (ordinary waves), the signal beam is shifted in x-axis from the center, Fig. 10a, where the pump beam is placed (red cross in the Figure). As a result, in the λ, θ_x space, the signal spectrum profile is non-symmetric, Fig. 10b. Due to the spatial walk-off, the conversion efficiency curves saturate already at $z = 0.75$ cm, Fig. 9. We note, that the spatial walk-off influence could be reduced by expanding pump beam radius. However, we preserve smaller pump beam radius with higher peak intensity.

In Fig. 11, the signal pulse profile and spectrum are depicted. At the second stage, the measured and numerically estimated signal pulse duration is around 400 ps (FWHM) and its numerical spectrum bandwidth at $\theta_x = \theta_y = 0$ is about 0.5 nm. In Fig. 11a, the numerical pump and idler pulse profiles are presented as well. Here, we observe that the pump wave is significantly depleted. As we can see from Figs. 10b and 11b, the frequency spectrum profile depends on the angle θ_x value. The experimental spectrum represents the integrated result, black line in Fig. 11b. The experimental signal spectrum was measured with an optical spectrometer "Avantes ULSC2048CL", while the output power was measured with "Ophir PD300-UV" power sensor. The experimental signal pulse duration

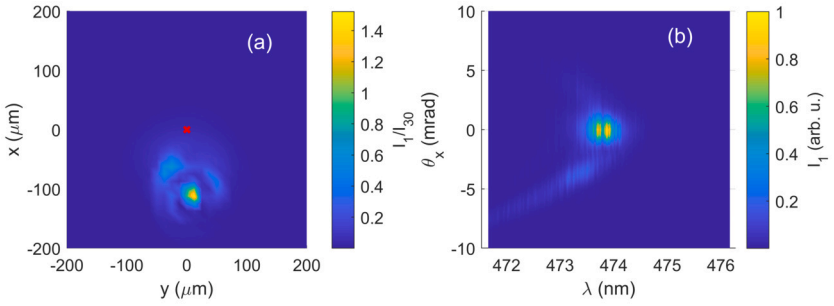

Fig. 10. Signal beam profile at $t = 0$ (a) and angular-frequency spectrum at $\theta_y = 0$ (b). $z = 0.75$ cm. Red cross in (a) – position of the pump beam. Numerical simulation, second stage.

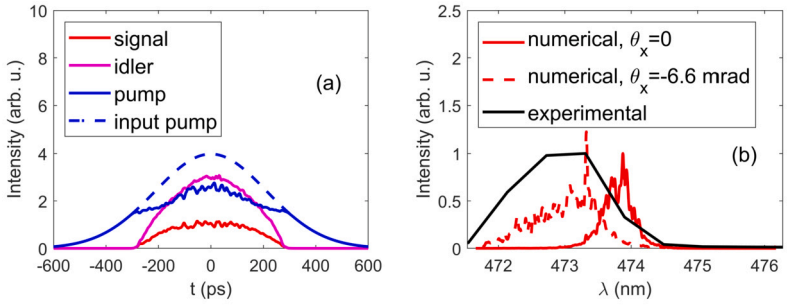

Fig. 11. Integrated over spatial coordinates output (solid lines) pulse profiles of signal, idler and pump waves as well as input (dashed line) pump pulse profile (a) and output signal frequency spectrum at $\theta_x = \theta_y = 0$ as well as at $\theta_x = -6.6$ mrad, $\theta_y = 0$ (b). Curves in (a) and red lines in (b): numerical simulation. Black curve in (b): experimentally measured signal spectrum. Second stage.

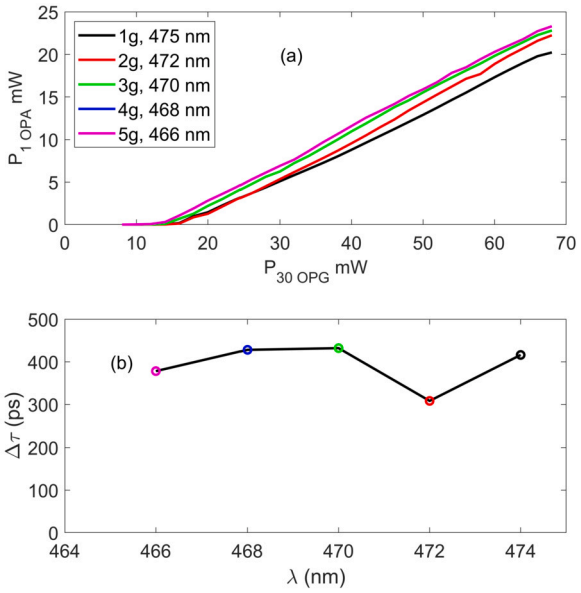

Fig. 12. (a) dependence of output OPA signal power on the input OPG pump power. (b) dependence of the OPA signal pulse duration (FWHM) on the central wavelength. First five gratings. Input OPA power $P_{30\text{OPA}} = 86$ mW. Experimental, second stage.

was evaluated using time-correlated single-photon counting (TCSPC) technique. In the experiment, the crystal length was $L = 1.5$ cm and the input pump power was 86 mW, while other parameters were the same as in the numerical simulation, Table 2. In Fig. 12a, we present the output signal power versus input first-stage pump power for the first five gratings. In the case of the first grating, the experimental conversion efficiency was 23% which is in good correspondence with the numerical result: about 20%, Fig. 9. The theoretical conversion efficiency to OPA signal wave is slightly smaller than the experimental one due to the sharp beam-center maximum of the seed beam, Fig. 5f. In the experiment, this maximum was smoothed due to the diffraction and therefore, larger part

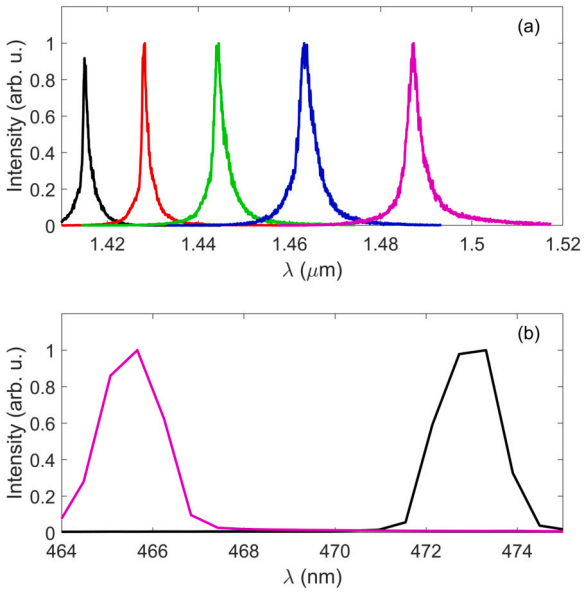

Fig. 13. Experimentally measured output signal spectra of first (a) and second (b) stages.

of the OPA pump beam profile was exploited. In Fig. 12a, the experimental values of the central signal wavelengths are provided, too. In Fig. 12b, the measured signal pulse duration is shown. As we can see, it does not vary significantly with the wavelength. Finally, in Fig. 13, the output OPG (a) and OPA (b) signal spectra are presented. The tuning in the visible wavelength range was achieved.

5. Discussion and conclusions

Subnanosecond two-stage optical parametric generation and amplification system under high conversion efficiency was studied. At the first stage, the input signal and idler noise waves mimic the quantum noise which intensity was calculated from the quantum model. We demonstrated that the number of input photons is not crucial if the corresponding propagation length shift is taken into account. The following simulation of the nonlinear coupling equations revealed the beam profile evolution of pump and signal waves. At first stage, the pump beam is depleted and further, it obeys the sharp maximum at the beam center. This sharp maximum arises due to the sharp maximum in the signal beam and the last is caused by the conical structure of the signal angular spectrum. We estimated the cone angles from the longitudinal phase-matching condition. We note, the observed conical sharp-maximum signal beam formation at optical parametric generation stage should be taken into account due to its influence on the laser-induced damage threshold. Such signal was utilized as a seed at the second-stage optical parametric amplifier. In the simulations, the pump beam radius was larger than the radius of the seed beam and therefore the conversion to the amplified signal beam was not optimal. The experimentally measured conversion efficiency was slightly larger. Due to the significant pump depletion at the first and second stages, large output second-stage signal power was observed both theoretically and experimentally. The tuning in the visible spectrum range has been achieved. Good qualitative agreement of experimental and theoretical results was obtained.

We believe that the described experimental setup provides an efficient and feasible way to achieve tunable wavelength subnanosecond duration pulses in the visible spectrum range. Moreover, our approach of the theoretical description of optical parametric generation will be useful in the future investigations of subnanosecond parametric systems, and practical applications such as pump-probe spectroscopy, skin disease treatment and other biomedical applications.

CRediT authorship contribution statement

V. Tamulienė: Writing – original draft, Supervision, Investigation. **G. Stanionytė:** Investigation. **T. Latvys:** Writing – review & editing, Investigation. **J. Vengelis:** Writing – review & editing, Supervision, Investigation.

Declaration of competing interest

The authors declare that they have no known competing financial interests or personal relationships that could have appeared to influence the work reported in this paper.

Data availability

Data will be made available on request.

Acknowledgement

This research has been carried out in the framework of the "Universities' Excellence Initiative" programme by the Ministry of Education, Science and Sports of the Republic of Lithuania under the agreement with the Research Council of Lithuania (project No. S-A-UEI-23-6).

Gabrielė Stanionytė is grateful to Jonas Banys for his advice.

References

[1] J.J. Zayhowski, A. Mooradian, Single-frequency microchip Nd lasers, Opt. Lett. 14 (1) (1989) 24–26, https://doi.org/10.1364/OL.14.000024.
[2] J.J. Zayhowski, J. Ochoa, A. Mooradian, Gain-switched pulsed operation of microchip lasers, Opt. Lett. 14 (23) (1989) 1318–1320, https://doi.org/10.1364/OL.14.001318.
[3] J.J. Zayhowski, Passively Q-switched Nd: YAG microchip lasers and applications, J. Alloys Compd. 303–304 (2000) 393–400, https://doi.org/10.1016/S0925-8388(00)00647-2.
[4] B.C. Castle, K. Visser, B.W. Smith, J.D. Winefordner, Spatial and temporal dependence of lead emission in laser-induced breakdown spectroscopy, Appl. Spectrosc. 51 (7) (1997) 1017–1024.
[5] J. Vengelis, V. Jarutis, V. Sirutkaitis, Visible supercontinuum generation in photonic crystal fiber using various harmonics of subnanosecond Q-switched laser, Opt. Eng. 55 (9) (2016) 096107, https://doi.org/10.1117/1.OE.55.9.096107.
[6] R. Bhandari, N. Tsuji, T. Suzuki, M. Nishifuji, T. Taira, Efficient second to ninth harmonic generation using megawatt peak power microchip laser, Opt. Express 21 (23) (2013) 28849–28855, https://doi.org/10.1364/OE.21.028849.
[7] L. Liu, H.Y. Wang, Y. Ning, C. Shen, L. Si, Y. Yang, Q.L. Bao, G. Ren, Sub-nanosecond periodically poled lithium niobate optical parametric generator and amplifier pumped by an actively Q-switched diode-pumped Nd: YAG microlaser, Laser Phys. 27 (5) (2017) 055403, https://doi.org/10.1088/1555-6611/aa6589.
[8] H. Qiao, K. Zhong, F. Li, X. Zhang, S. Wang, Y. Zheng, D. Xu, Q. Sheng, W. Shi, J. Yao, Efficient MW-peak-power kHz-repetition-rate sub-nanosecond optical parametric generator tunable from near- to mid-infrared, Opt. Laser Technol. 151 (2022) 108010, https://doi.org/10.1016/j.optlastec.2022.108010.
[9] K. Zhong, H. Qiao, F. Li, X. Zhang, Y. Zheng, S. Wang, D. Xu, J. Yao, Tunable narrow-linewidth high-peak-power sub-nanosecond optical parametric generator by injection seeding, Opt. Express 30 (10) (2022) 16479–16488, https://doi.org/10.1364/OE.457852.
[10] J. Banys, J. Savickytė, O. Balachninaitė, S. Armalytė, V. Tamulienė, V. Jarutis, J. Vengelis, Performance investigation of high-efficiency widely tunable sub-nanosecond optical parametric generator and amplifier based on MgO:PPLN, Opt. Express 30 (13) (2022) 23163–23176, https://doi.org/10.1364/OE.459826.
[11] G. Marchev, P. Dallocchio, F. Pirzio, A. Agnesi, G. Reali, V. Petrov, A. Tyazhev, V. Pasiskevicius, N. Thilmann, F. Laurell, Sub-nanosecond, 1–10 khz, low-threshold, non-critical opos based on periodically poled KTP crystal pumped at 1,064 nm, Appl. Phys. B 109 (2012) 211–214, https://doi.org/10.1007/s00340-012-5177-4.
[12] A.C. Chiang, Y.C. Huang, Y.W. Fang, Y.H. Chen, Compact, 220-ps visible laser employing single-pass, cascaded frequency conversion in monolithic periodically poled lithium niobate, Opt. Lett. 26 (2) (2001) 66–68, https://doi.org/10.1364/OL.26.000066.
[13] S. Acco, P. Blau, A. Arie, Output power and spectrum of optical parametric generator in the superfluorescent regime, Opt. Lett. 33 (11) (2008) 1264–1266, https://doi.org/10.1364/OL.33.001264.
[14] P.E. Powers, J.W. Haus, Fundamentals of Nonlinear Optics, CRC Press, Boca Raton, 2017.
[15] L. Carrion, J.-P. Girardeau-Montaut, Development of a simple model for optical parametric generation, J. Opt. Soc. Am. B 17 (1) (2000) 78–83, https://doi.org/10.1364/JOSAB.17.000078.
[16] O. Paul, A. Quosig, T. Bauer, M. Nittmann, J. Bartschke, G. Anstett, J.A. L'Huillier, Temperature-dependent Sellmeier equation in the MIR for the extraordinary refractive index of 5% MgO doped congruent $LiNbO_3$, Appl. Phys. B 86 (2007) 111–115, https://doi.org/10.1007/s00340-006-2414-8.
[17] M.S. Wartak, Computational Photonics: An Introduction with MATLAB, Cambridge University Press, United Kingdom, 2013.
[18] P. Di Trapani, A. Beržanskis, S. Minardi, S. Sapone, W. Chinaglia, Observation of optical vortices and J_0 Bessel-like beams in quantum-noise parametric amplification, Phys. Rev. Lett. 81 (23) (1998) 5133–5136, https://doi.org/10.1103/PhysRevLett.81.5133.
[19] S. Lin, Y. Tanaka, S. Takeuchi, T. Suzuki, Improved dispersion equation for mgo:linbo$_3$ crystal in the infrared spectral range derived from sum and difference frequency mixing, IEEE J. Quantum Electron. 32 (1) (1996) 124–126, https://doi.org/10.1109/3.481928.
[20] D.N. Nikogosyan, Nonlinear Optical Crystals: A Complete Survey, Springer, Ireland, 2005.